Physics in Medicine & Biology

PAPER

Investigating beam range uncertainty in proton prostate treatment using pelvic-like biological phantoms

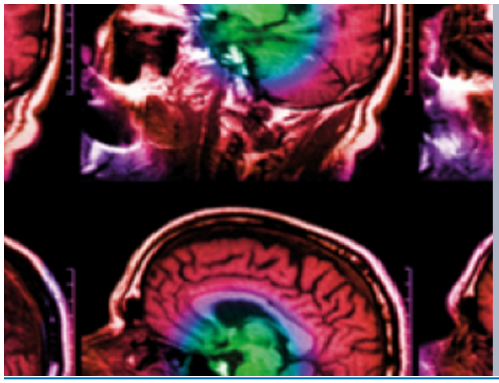

Physics in Medicine & Biology

IPEM Institute of Physics and Engineering in Medicine

RECEIVED
31 May 2021

REVISED
19 August 2021

ACCEPTED FOR PUBLICATION
25 August 2021

PUBLISHED
9 September 2021

PAPER

Investigating beam range uncertainty in proton prostate treatment using pelvic-like biological phantoms

Wencheng Shao[1,2,3], **Yunhe Xie**[2,8], **Jianan Wu**[4,5,8], **Liyan Zhang**[6], **Schuemann Jan**[2] and **Hsiao-Ming Lu**[2,7]

[1] Department of Nuclear Science and Technology, Nanjing University of Aeronautics and Astronautics, Nanjing, People's Republic of China
[2] Division of Radiation Biophysics, Department of Radiation Oncology, Massachusetts General Hospital and Harvard Medical School, Boston, United States of America
[3] Department of Radiation Physics, Harbin Medical University Cancer Hospital, Harbin, People's Republic of China
[4] Department of Radiation Oncology, National Cancer Center/National Clinical Research Center for Cancer/Cancer Hospital & Shenzhen Hospital, Chinese Academy of Medical Sciences and Peking Union Medical College, Shenzhen, People's Republic of China
[5] Institute of Biomedical and Health Engineering, Shenzhen Institutes of Advanced Technology, Chinese Academy of Sciences, Shenzhen, People's Republic of China
[6] Department of Engineering Physics, Tsinghua University, Beijing, People's Republic of China
[7] Hefei Ion Medical Center and Ion Medical Research Institute, University of Science and Technology of China, Hefei, People's Republic of China
[8] These authors contributed to the work equally and are regarded as co-first authors.

E-mail: hmlu@himc.org.cn

Keywords: proton therapy, range uncertainty, WEPL, dose extinction

Abstract

This study aims to develop a method for verifying site-specific and/or beam path specific proton beam range, which could reduce range uncertainty margins and the associated treatment complications. It investigates the range uncertainties from both CT HU to relative stopping power conversion and patient positioning errors for prostate treatment using pelvic-like biological phantoms. Three $25 \times 14 \times 12\ cm^3$ phantoms, made of fresh animal tissues mimicking the pelvic anatomies of prostate patients, were scanned with a general electric CT simulator. A 22 cm circular passive scattering beam with 29 cm range and 8 cm modulation width was used to measure the water equivalent path lengths (WEPL) through the phantoms at multiple points using the dose extinction method with a MatriXXPT detector. The measured WEPLs were compared to those predicted by TOPAS simulations and ray-tracing WEPL calculations. For the three phantoms, the WEPL differences between measured and theoretical prediction (WDMT) are below 1.8% for TOPAS, and 2.5% for ray-tracing. WDMT varies with phantom anatomies by about 0.5% for both TOPAS and ray-tracing. WDMT also correlates with the tissue types of a specific treated region. For the regions where the proton beam path is parallel to sharp bone edges, the WDMTs of TOPAS and ray-tracing respectively reach up to 1.8% and 2.5%. For the region where proton beams pass through just soft tissues, the WDMT is mostly less than 1% for both TOPAS and ray-tracing. For prostate treatments, range uncertainty depends on the tissue types within a specific treated region, patient anatomies and the range calculation methods in the planning algorithms. Our study indicates range uncertainty is less than 2.5% for the whole treated region with both ray-tracing and TOPAS, which suggests the potential to reduce the current 3.5% range uncertainty margin used in the clinics by at least 1% even for single-energy CT data.

1. Introduction

Prostate cancer is a malignant disease that threatens healthy men around the world (Al-Abdin and Al-Beeshi 2018, Góes *et al* 2018, Joachim *et al* 2018). Proton therapy is an effective method to treat prostate tumor with lower toxicity to organs at risk and normal tissues because of the dosimetric characteristics of proton Bragg

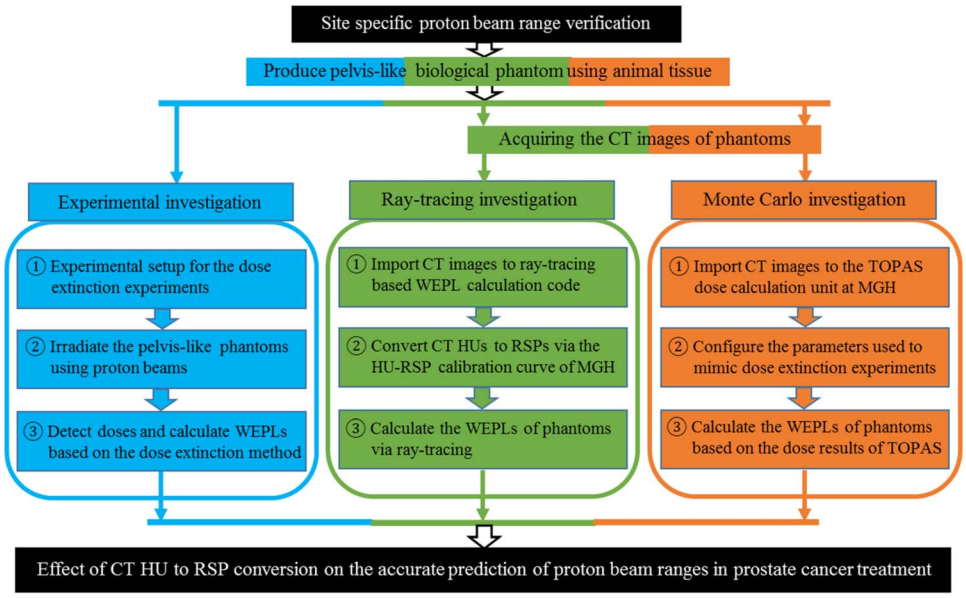

Figure 1. Work flow for verifying site-specific proton beam range in prostate cancer treatment.

Peaks (Mendenhall *et al* 2012, Paganetti and Kooy 2014, Guan *et al* 2015, Shao *et al* 2017). There are two obvious characteristics for the proton transportation during prostate cancer treatment. First, the proton transportation path almost reaches up to 30 cm. Second, the proton beams pass through a large bone before reaching the treated site. The two characteristics introduce two extra problems for prostate treatment. First, larger range uncertainty could result because of the integral effect of CT HU to relative stopping power (RSP) conversion uncertainty along the long transportation path. Second, range uncertainty can be aggravated in presence of the large bone along the transportation path (Yang *et al* 2012).

In proton therapy, the range uncertainties from CT HU to RSP conversion and patient positioning error are two of the challenges to accurate beam range prediction (Paganetti 2012, Liebl *et al* 2014, Schuemann *et al* 2014, Zheng *et al* 2016, Tryggestad *et al* 2020). The consistency between measured WEPLs and theoretically predicted WEPLs is an effective reference to reflect whether CT HU to RSP conversion is sufficiently accurate for predicting beam range. Existing studies have investigated the range uncertainty from CT HU to RSP conversion based on uniform biological tissues or generic mixtures of tissue types (Doolan *et al* 2015, Zhang *et al* 2017). However, for prostate treatment, the treated site is surrounded by skin, fat, muscle, and bone, etc, and the beams travel through multiple types of biological tissues arranged in specific proportions for the treated site. The conclusions of existing studies cannot be directly applicable to practical prostate treatment. It is thus necessary to study the range uncertainty for prostate treatment using pelvic-like biological phantoms mimicking prostate patients' pelvic anatomy.

2. Materials and methods

In this study, the experiments, ray-tracing calculation and TOPAS simulation were performed at Massachusetts General Hospital (MGH). As exhibited in figure 1, the general work flow of this study was segmented into the blue, green, and orange branches. The blue branch was adopted to measure the WEPLs of the phantoms based on dose extinction experiments. The green branch aimed to derive WEPLs from the CT images of the phantoms through ray-tracing. The orange branch was introduced to calculate WEPLs via TOPAS simulation.

2.1. Configuration of pelvic-like phantoms

The strategy for configuring the phantom was inspired by the actual pelvic anatomy shown in figure 2(a). The conceptual geometry of the phantom was illustrated in figure 2(b). During this study, 8 phantoms were produced. The first 5 phantom were used to practice how to produce the phantom as stable as possible within the shortest time as phantom producing exercises. The first 5 phantoms were also scanned by the general electric (GE) CT simulator and evaluated to improve the skill for producing phantoms as close to human pelvic anatomy as possible. The last 3 phantoms were used to perform the dose extinction experiments. Each phantom was manually produced by fresh animal tissues to mimic the pelvic anatomies of prostate cancer patients. For the three phantoms, the skin, fat, muscle, and bone regions were respectively produced by pig skin, pig fat, pig

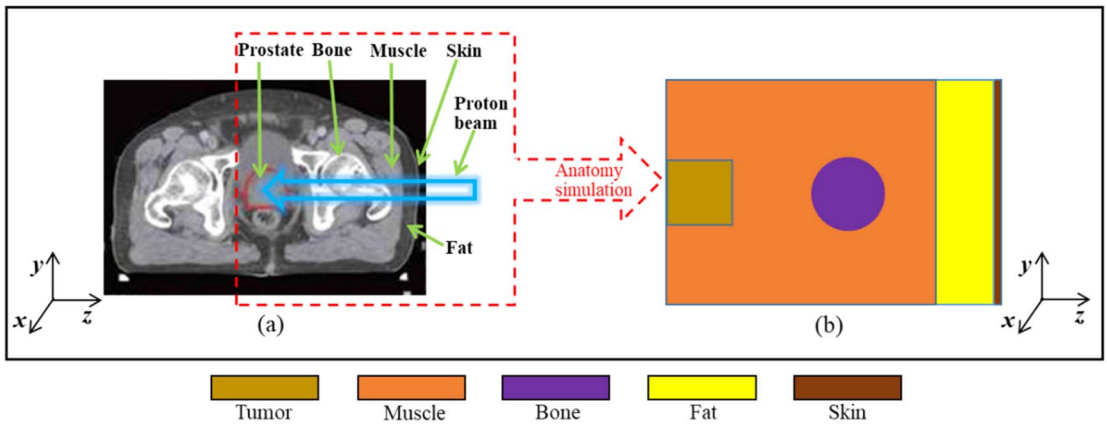

Figure 2. Conceptual strategy for configuring the pelvic-like phantoms: (a) real anatomy relevant to proton treatment of prostate cancer; (b) phantom configuration in *y*–*z* plane. This configuration is a conceptual design, and it may be slightly different from the practically produced phantoms.

Table 1. Geometric extents in *x*, *y*, and *z* for the pelvic-like biological phantoms.

	Maximum sizes (cm)				
Axis	Pig skin	Pig fat	Pig muscle	Femoral head	Tumor
x	10	10	10	4	4
y	12	12	12	4	4
z	0.4	3	21.6	4	4

muscle and pig femoral head. All the fresh pig tissues were wrapped in a $25 \times 14 \times 12\ \text{cm}^3$ cuboid container to keep the tissues stable. The phantoms were made of fresh animal tissues purchased from a local market. For each phantom, the tissues were placed in a $25 \times 14 \times 12\ \text{cm}^3$ cuboid container to keep the phantom structure stable. Inside the container, the tissues were immersed in salt water with 0.9% salt concentration to keep the tissues stable throughout the CT scan and dose extinction experiment. The entire experimental process from animal tissue acquisition to its disposal was completed in the same day to avoid freezing the animal tissues. Table 1 listed the approximate geometric extents of the fresh pig tissues wrapped in the cuboid container.

2.2. CT imaging

The phantoms were respectively scanned by a single-energy GE CT simulator to acquire the CT data required by Monte Carlo (MC) simulation and ray-tracing calculation. The voxel size of $0.97 \times 0.97 \times 1.25\ \text{mm}^3$ was used for the CT scans. The tube current of 200 mA was applied with the scan voltage set at 140 kV. The CT images of the phantoms were selectively shown in figure 3.

2.3. WEPL measurements based on dose extinction

In this study, a dose extinction based WEPL measuring method (Betefour *et al* 2015) was performed to measure the WEPLs through the pelvic-like phantoms in the G1 treatment room at MGH. Figure 4 exhibits the experiment setup of dose extinction based WEPL measurement including a passive scattering snout, a phantom, solid water slabs and MatriXXPT. MatrXXPT is a two-dimension dose detecting array dedicated to dose measurements in proton therapy. The distance between proton source and iso-center is 248 cm, and the distance between the downstream phantom surface and detector surface is 5 cm. The gantry angle of the therapy machine was set as 90°.

In general, the WEPL measuring method adopts the fact that the beam range in our system is defined as the distance from the surface of the water tank to the 90% dose level on the distal dose falloff and is calibrated within 0.5 mm. To obtain the WEPL from the phantom surface to the dose detecting location (WEPL_{pd}), one only needs to obtain the beam range (R_{pd}) which delivers 90% of the dose relative to the dose plateau of the SOBP. In detail, during dose extinction experiments, the passive scattering beam with 29 cm range with 8 cm modulation width was applied to horizontally irradiate the phantom. Labeled solid water slabs with the WEPLs of 0.21, 0.22, 0.23, 0.55, 1, and 2.03 cm were inserted between the phantom and MatriXXPT. By the combination of those 6

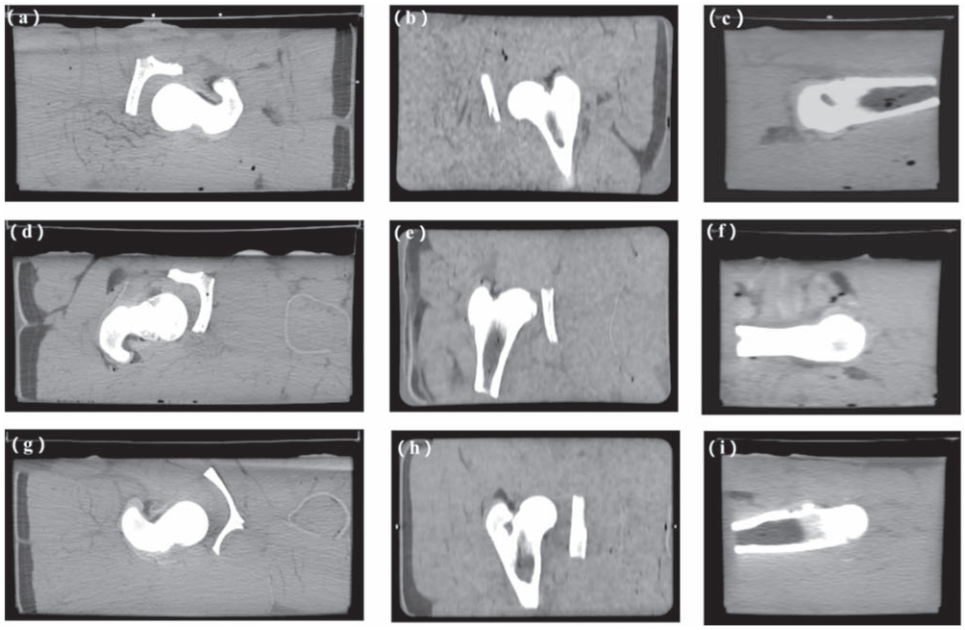

Figure 3. CT images of phantom 1 (a)–(c), phantom 2 (d)–(f) and phantom 3 (g)–(i) in *y*–*z*, *x*–*z*, and *x*–*y* planes.

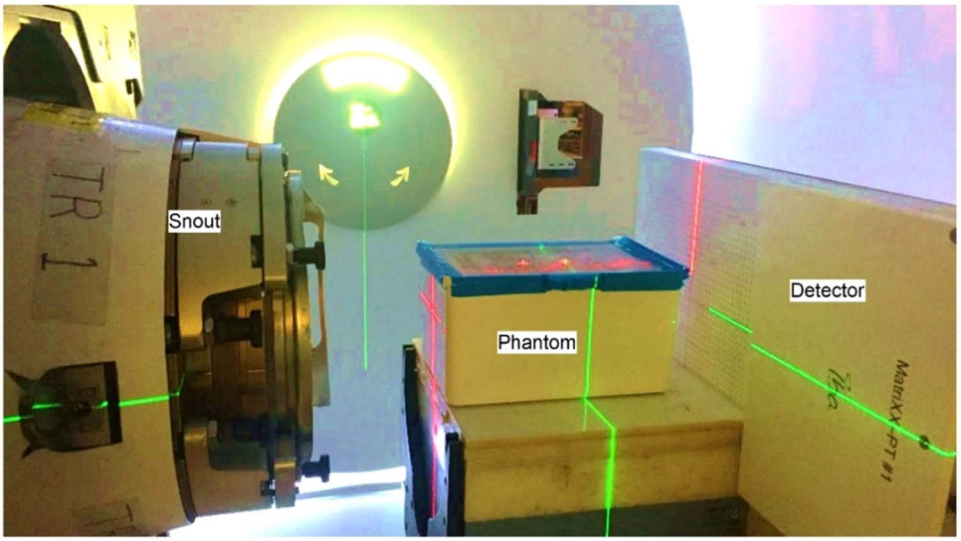

Figure 4. The dose extinction experiment setup for measuring the WEPLs through the phantom.

solid slabs, 18 solid water thicknesses can be achieved. The WEPLs corresponding to the 18 thicknesses respectively are 0.21, 0.43, 0.55, 0.66, 0.76, 1, 1.21, 1.43, 1.55, 1.66, 1.76, 2.03, 2.24, 2.46, 2.58, 2.69, 2.79 and 3.03 cm. For each solid slab thickness, 100 MUs protons were delivered, and the exiting doses downstream of the phantom were recorded by MatriXXPT. The detectors in the MatriXXPT detecting array obtained a two-dimension dose distribution for each 100 MUs dose delivery. For a specific slab thickness, all the detectors detected the exiting dose downstream of the phantom at the same time. Thus, we did not need to repeat the procedure for each detector. Solid slab thicknesses were gradually increased until the dose went down to zero and the 90% of the dose relative to the SOBP dose plateau was identified to obtain R_{pd}. Assuming the solid slab WEPL corresponding to 90% dose falloff is $WEPL_{sl}$, the WEPLs through the phantom ($WEPL_{pd}$) can be calculated as follows:

$$WEPL_{pd} = R_{pd} - WEPL_{sl}. \quad (1)$$

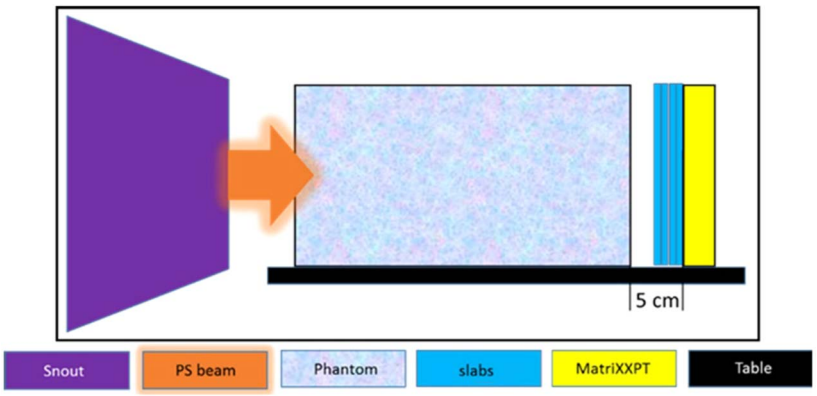

Figure 5. Virtual experiment setup for dose extinction simulation via TOPAS.

2.4. WEPL calculation via MC simulation

As exhibited in figure 5, a virtual dose extinction experiment was simulated using TOPAS (Ver. 3.4), exactly based on the experiment setup described in section 2.3. (Testa et al 2013) In detail, a virtual proton therapy machine with 90° gantry angle was constructed exactly per the geometric and physical parameters of the IBA machine at MGH. Thus the virtual IBA machine could generate the virtual proton beam with the physical parameters exactly as in the real experiment. The CT images of the phantom were imported into TOPAS to construct the virtual phantom for MC simulation. The 237 mm × 237 mm virtual detector array with 1 mm pixel size was placed downstream from the phantom. The iso-center of the beam with 29 cm range with 8 cm modulation width was set at the origin of the CT HU matrix, just as in the actual measurements.

In detail, water slabs with different WEPLs were inserted into the gap between the phantom and detector array. The WEPLs of the water slabs respectively are 0.21, 0.43, 0.55, 0.66, 0.76, 1, 1.21, 1.43, 1.55, 1.66, 1.76, 2.03, 2.24, 2.46, 2.58, 2.69, 2.79 and 3.03 cm. The locations of the phantom and MatriXXPT were kept the same, the slab thickness was gradually increased until the doses went down to zero, and the 90% dose was identified from the SOBP dose falloff region to obtain R_{pd} and $WEPL_{sl}$ (Wang *et al* 2017). One MC simulation run was performed for each solid slab thickness with 10^9 events. Then the WEPLs through the phantom ($WEPL_{pd}$) were calculated per equation (1). The TOPAS MC simulations were performed on the ERISOne scientific computation sever of Mass General Brigham. The statistical uncertainties of MC calculated dose were less than 2%.

2.5. WEPL calculation via ray-tracing

In this study, the ray-tracing-predicted WEPLs through the phantoms were calculated using the WEPL calculation function of the pXiO planning system which wasused for passive scattering proton treatment at MGH. The CT images of the phantoms were imported to pXiO to construct the geometric configuration. As seen in figure 6, for pXiO the WEPLs through the phantom were calculated by adding up the WEPLs of all the CT voxels along the straight proton track between points A and B; the calculated WEPLs were recorded at point C (scoring point); the WEPL distribution on each scoring line was obtained when moving the point C along the scoring line with 1 mm step size. The WEPL of each CT voxel was calculated as the product of the RSP and the track length within the voxel. The RSP of each voxel was acquired through the CT HU to RSP conversion (Jiang *et al* 2007, De Marzi *et al* 2013, Ainsley and Yeager 2014, Brousmiche *et al* 2017) conversion curve used in clinics at MGH. As shown in figure 6(b), the WEPLs through the phantom were calculated on seven WEPL scoring lines. On each scoring line, there are 80 scoring points when setting the scoring spacing as 1 mm. For each phantom, the seven scoring lines for calculating WEPLs using the pXiO are respectively named as scoring lines 1–7 in the order from left to right. The fourth line passes through the projection of iso-center on the WEPL calculating plane. The distance between two adjacent scoring lines is 1 cm. The authors limited the WEPL calculation to only the points along the 7 scoring lines, instead of obtaining a high resolution 2D distribution as those obtained from TOPAS simulations, because the WEPL calculation in pXio is entirely manual and can only be done one point at a time. The ray-tracing WEPL calculation of pXiO planning system requires the users to manually input the coordinate values for each WEPL calculating track. The users need to use at least 700 h by manually inputting parameters when aiming to calculate the whole two-dimension WEPLs via pXiO ray-tracing for just one phantom. Thus 7 lines were selected to represent the WEPLs, which makes the pXiO ray-tracing calculation feasible.

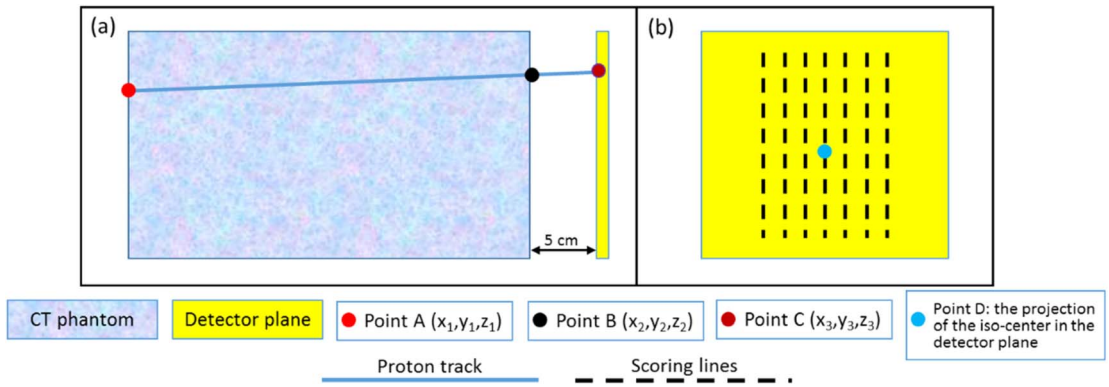

Figure 6. Geometric configuration for ray-tracing WEPL calculation using pXiO: (a) the configuration of the ideal straight proton track and the red, black and brown points where the track meets the phantom surfaces and detector surface in the *y*–*z* plane; (b) the configuration of the detecting plane, the projection of the iso-center and WEPL scoring lines in *x*–*y* plane. The iso-center of the proton beam is set at the origin of the CT HU matrix according to the dose extinction experiment setup. The source-axis distance (SAD) is 248 cm for the beam option used in the measurement. The proton source point and points A–C are located on one straight proton track.

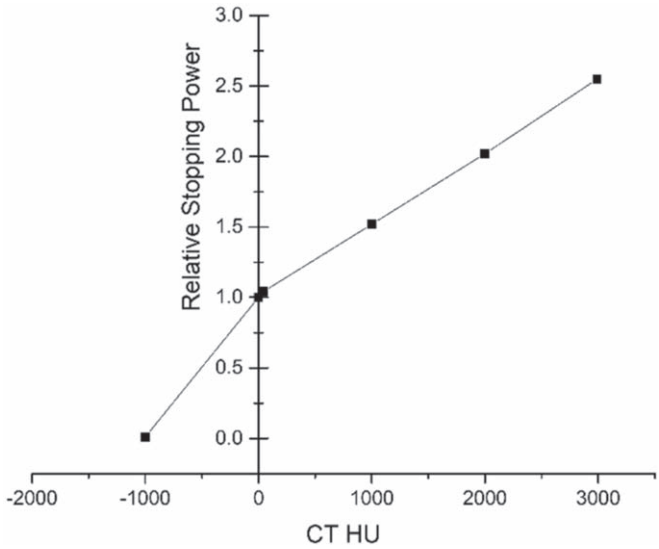

Figure 7. Illustration of the MGH-specific HU to RSP conversion curve.

2.6. CT HU to RSP conversion

For ray-tracing WEPL prediction, the CT HU of prostate cancer patients needs to be converted to RSPs before dose calculation. CT HU to RSP conversion is required for typical treatment planning systems (TPSs). Figure 7 shows the CT HU to RSP conversion curve used by this study. This conversion curve is applied in clinical proton therapy at MGH, and is used to convert CT HU to RSP before calculating WEPLs through the three phantoms by using pXiO. For TOPAS MC simulation, CT HUs of the phantoms were respectively converted to tissue densities and elemental weights according to Schneider's study (Schneider *et al* 2000).

2.7. Coordinating scoring positions between different WEPL predicting methods

During the dose extinction experiments, the position of the projection of iso-center was identified and marked on the WEPL scoring plane. For TOPAS and ray-tracing, WEPLs through the phantom were set up under the same three-dimensional coordinate system exactly as in the experiment for each specific phantom. The origin of the scoring coordinate system was set at the projection of iso-center on the WEPL scoring plane. Each scoring point has a unique scoring position which is the same for experiments, TOPAS and ray-tracing. When comparing WEPLs between two WEPL predicting ways, we just need to compare the two WEPL values for the two ways at each specific position.

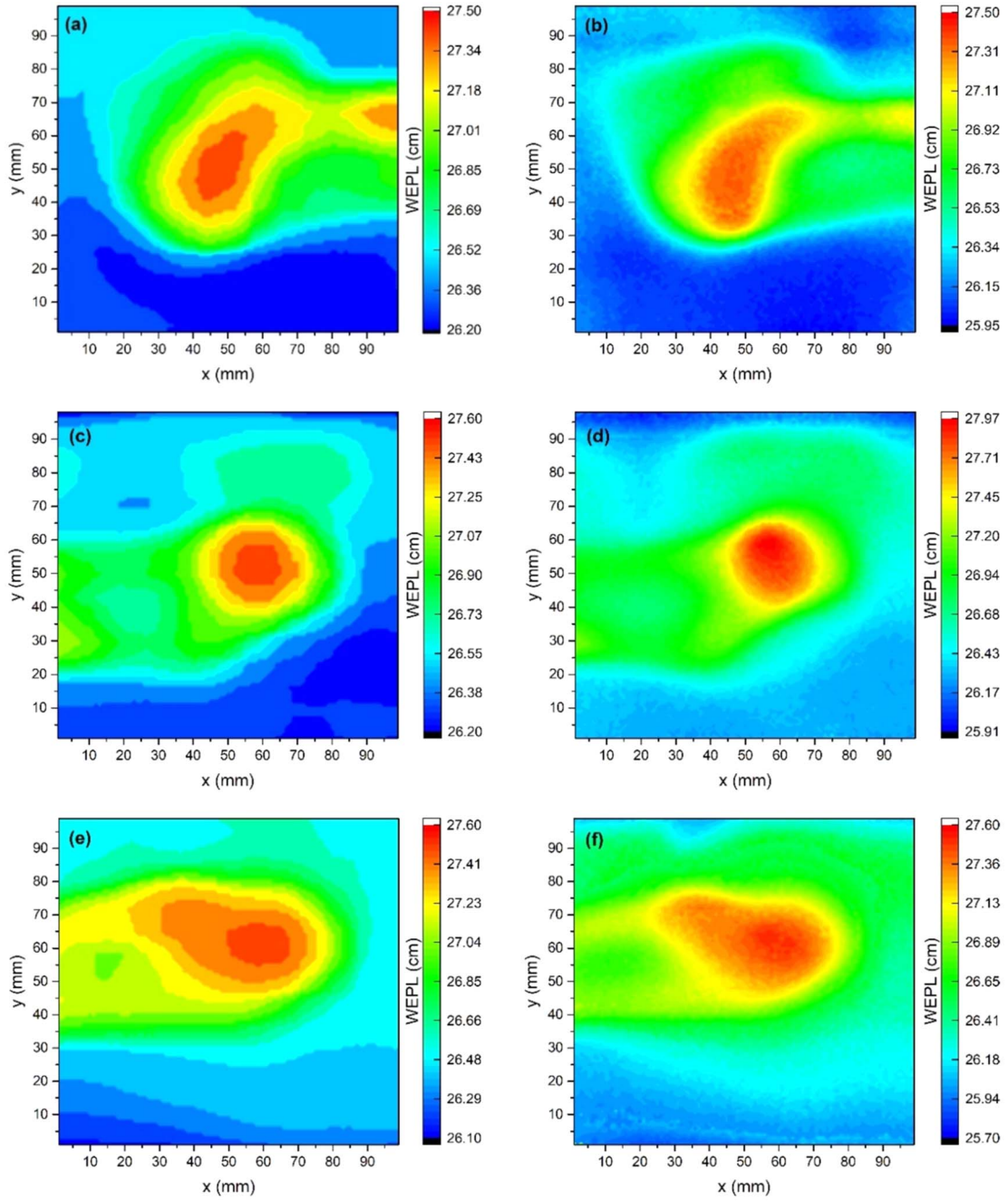

Figure 8. Measured WEPLs from the dose extinction experiments versus TOPAS-predicted WEPLs for (a), (b) phantom 1, (c), (d) phantom 2 and (e), (f) phantom 3. Figures a, c and e show the measured WEPLs and figures b, d and f display the TOPAS-predicted WEPLs.

3. Results

The measured- and TOPAS-predicted WEPLs are shown in figure 8. The differences between measured- and TOPAS-predicted WEPLs were plotted in figure 9, while those between the measured- and ray-tracing-predicted WEPLs are displayed in figure 10. In figures 8 and 9, the exhibiting region of 10 cm $\times$ 10 cm was selected to include both the bone and surrounding tissues. For prostate treatments, the beam cross sections are usually less than 10 $\times$ 10 cm^2, and therefore the selected area is adequate to cover the whole irradiated region involved in practical prostate treatments. As seen in figure 8, the measured and TOPAS calculated WEPLs through the three phantoms ranged from 26 to 28 cm, with the largest WEPL around the boney area and the smallest in the soft tissue region.

Figure 9 shows histograms of WEPL discrepancies between the measurements and TOPAS predictions for the three phantoms. As seen in figure 9, the discrepancy range of −0.5% to 1.5% was observed for phantom 1,

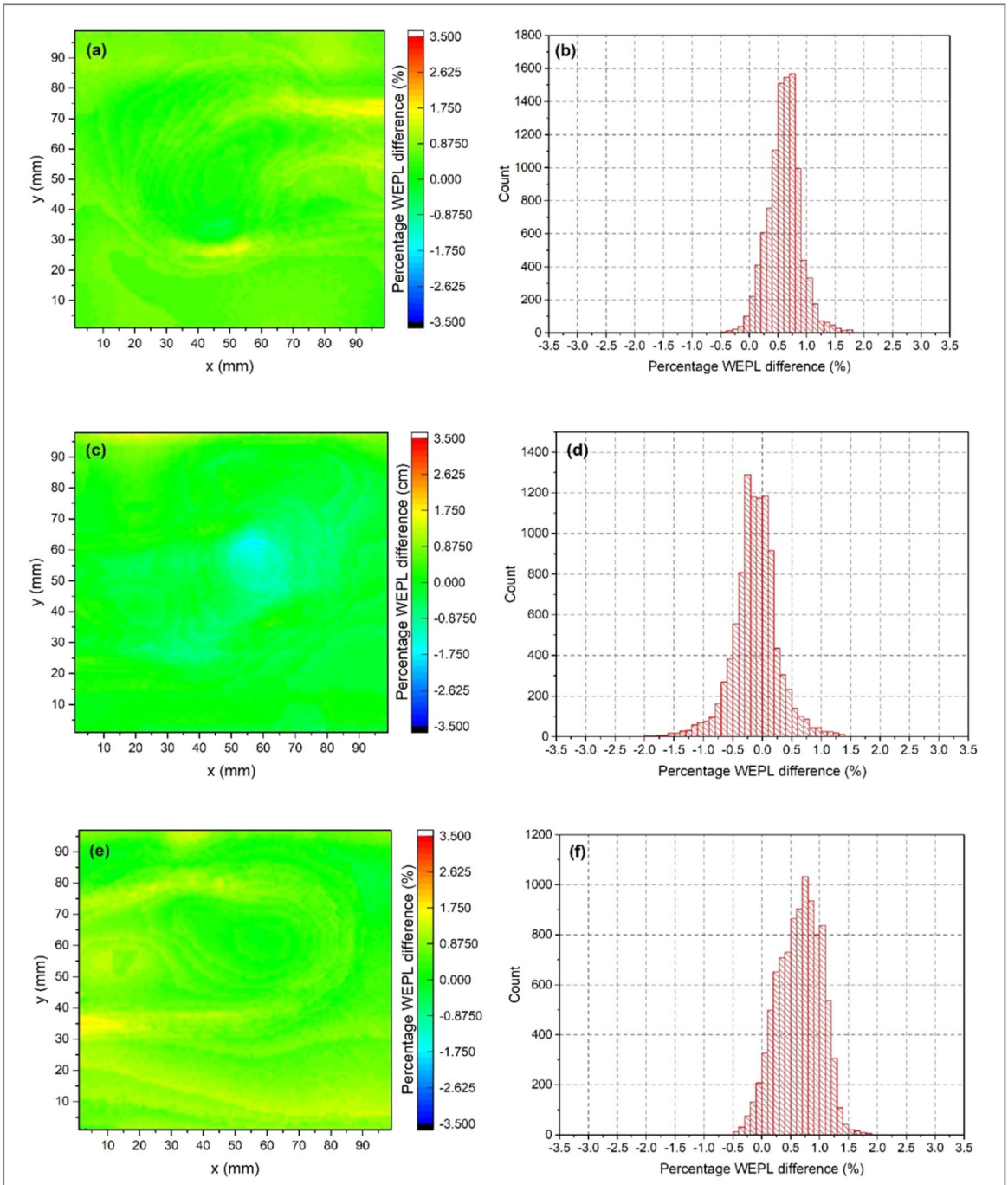

Figure 9. WEPL difference between measured- and TOPAS-predicted WEPLs in *x*–*y* plane: (a) the 2D difference map for phantom 1; (b) the histogram of WEPL difference for phantom 1; (c) the 2D difference map for phantom 2; (d) the histogram of WEPL difference for phantom 2; (e) the 2D difference map for phantom 3; (f) the histogram of WEPL difference for phantom 3. The percentage WEPL difference was defined as the difference between measured- and TOPAS-predicted WEPLs, divided by the proton range of 29 cm, multiplied by 100. It reflects the percentage uncertainty of predicting WEPLs with TOPAS simulation. (The count in figures 9(b), (d) and (f) stands for the quantity of 1 mm^2 regions within a specific percentage WEPL difference bin.)

−1.5% to 1.5% for phantom 2, −0.5% to 1.8% for phantom 3. The most probable WEPL discrepancy were about 0.5%, 0%, and 0.7% for phantoms 1–3, respectively.

Figure 10 shows the percentage WEPL differences between measured- and ray-tracing-predicted WEPLs for the three phantoms. The maximum percentage WEPL differences for all the three phantoms were 2.5%. It is found that these high discrepancy points occurred where the WEPL calculation paths pass through regions near bone edges. Figure 11 compares the WEPLs from ray-tracing, TOPAS MC and experiment at points along a scoring line across the bone edges in phantom 3. As shown in figure 11(b), the WEPLs from ray-tracing showed sharp peaks at the two hard bone edges and causing the discrepancy from measurements almost to 2.5%, whereas the WEPLs from TOPAS MC were much closer to the measurements. For ray-tracing, the proton track

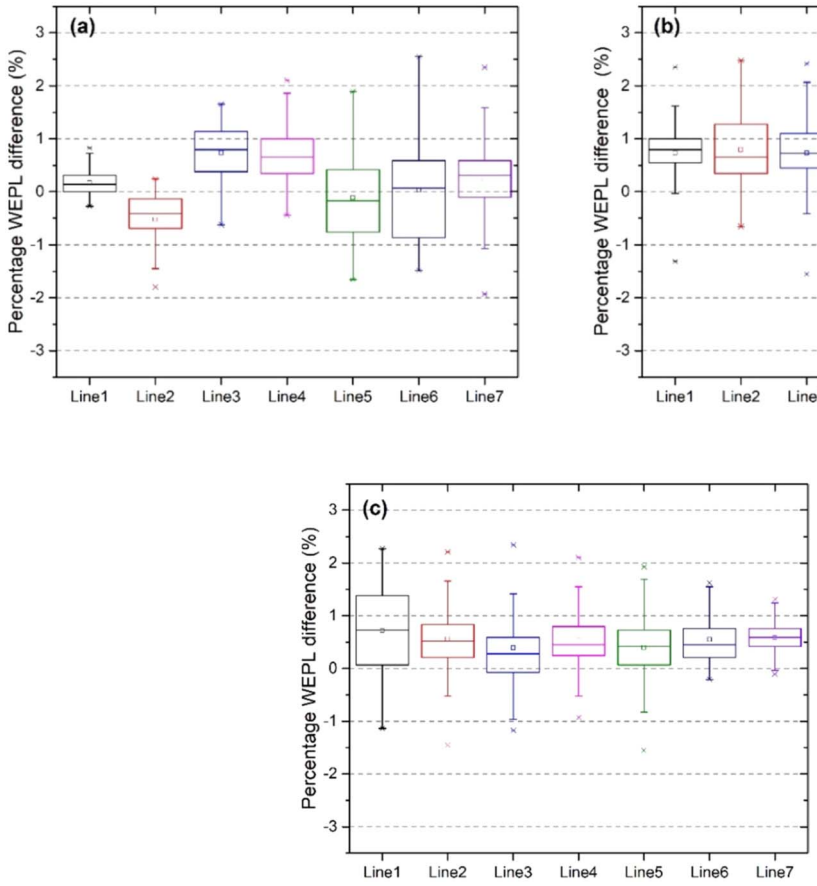

Figure 10. Box plots for the percentage WEPL difference between measured- and ray-tracing-predicted WEPLs on the seven WEPL scoring lines for (a) phantom 1, (b) phantom 2; (c) phantom 3. The percentage WEPL difference was defined as the difference between measured- and ray-tracing-predicted WEPLs, divided by the proton range of 29 cm, multiplied by 100. It reflects the percentage uncertainty of predicting WEPLs when using ray-tracing. Lines 1–7 denote the seven WEPL scoring lines (see figure 8) for calculating ray-tracing WEPLs using pXiO.

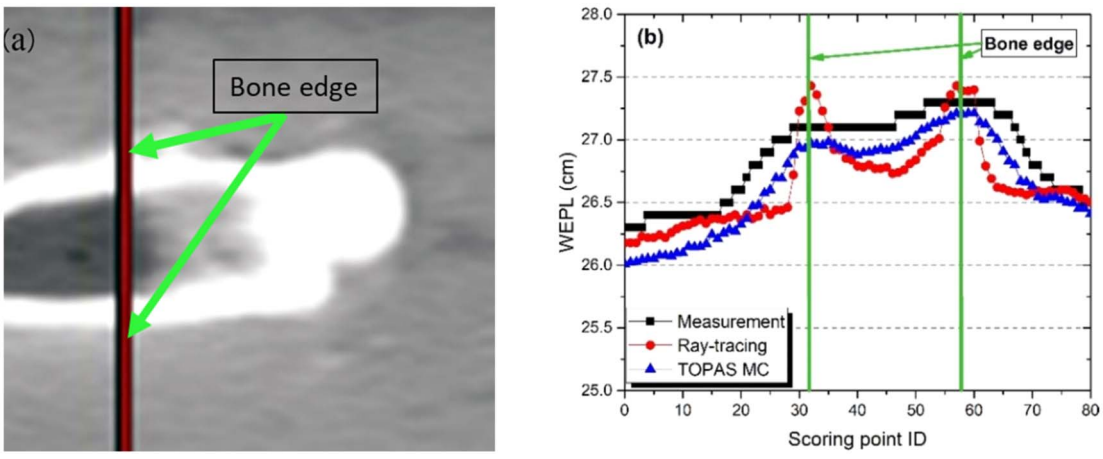

Figure 11. Illustrations for showing why the percentage WEPL difference from ray-tracing reaches up to 2.5%: (a) the overlapping view including the scoring line 1 and the CT snapshot for the treated region of phantom 3; (b) the calculated WEPLs from measurements, ray-tracing, and TOPAS on the scoring line 1 for phantom 3. The red line on figure 11(a) denotes the scoring line 1 which crosses sharp bone edges. (For measurements and TOPAS simulation, the scoring point IDs is converted from the scoring positions relative to the ray-tracing scoring positions on scoring line 1.)

was deemed as ideal straight line when calculating WEPL through the phantom, and the range-mixing due to scattered protons around hard bone edges were not taken into account properly. This occurrence could be a possible reason for the larger discrepancy between ray-tracing and measured WEPLs.

Table 2. Mean HUs and standard deviations for the areas randomly selected from the muscle, fat and bone tissues of the phantom and real anatomy.

Tissue type	Source	MH	SD	Difference in MH	Difference in RSP (%)
Fat	Phantom	−67	23	23.85	1.7%
	Patient	−90.85	35.71		
Muscle	Phantom	54.24	19.21	15.84	1.1%
	Patient	70.08	34.68		
Femoral head	Phantom	419.38	59.75	17.62	1.2%
	Patient	437	105.62		

There are noticeable differences between patient and phantoms. In particular, the muscle HU peak of the real patient pelvic anatomy is lower and wider than those of the phantoms. To investigate, we randomly selected three circular areas with 1 cm diameter in the fat, muscle and bone tissues of both phantom 2 and the patient. The mean HUs (MHs) and standard deviations (SDs) for the selected areas were calculated and shown in table 2. As listed in table 2, the differences in MH between the patient and phantom 2 are respectively 23.85 HU, 15.84 HU and 17.62 HU for muscle, fat and femoral head. These differences would translate approximately to 1.7%, 1.1% and 1.2% differences in RSP for the three types of tissues, according to the CT HU to RSP conversion curve used in our clinic.

In this study, the beam range uncertainty in typical prostate treatment was investigated using pelvic-like phantoms made of fresh animal tissues. One of the concerns of the study is whether the pelvic-like phantoms can closely mimic real pelvic anatomy well. To address this, the CT HUs in the irradiated regions were respectively acquired and analyzed for phantoms 1–3 and were compared to those from the pelvic anatomy of a typical prostate patient selected from five prostate patients who underwent proton therapy at MGH. Figure 12 shows the CT HU histograms derived from the CT images of the prostate patient (a) and the three phantoms (b–d). As shown in figure 12, all four plots contain two peaks, one at about −80 HU and the other at about 50 HU, corresponding to fat and muscle tissues, respectively.

To verify the stability of the phantoms, phantom 3 was selected as an example and respectively scanned by the GE CT simulator before and after the dose extinction measurement. The time interval between the first CT scan and second CT scan was about 2.5 hours. Image fusion between the pre- and post-experiment CT sets was performed by aligning the container frames via Mim. The largest differences in CT HU appeared around the bone edges, indicating slight displacements of these bones. They mainly occurred in the longitudinal direction at about 1.5 mm maximum, as seen in the difference map of the CT HUs for one CT slice shown in figure 13. No significant HU differences were observed in other regions, which suggests that the phantom had been reasonably stable within the time frame of the experiments.

4. Discussion

Proton beam range uncertainty has been a major challenge to fully realizing the potential benefits of proton beam therapy. Current clinical practice employs a sizable range margin in order to ensure target coverage, while risking unnecessary dose deposition to normal tissues behind the target volume. In most clinics, the same margin recipe is used for all treatment sites, with its main component from uncertainties in the CT HU to RSP conversion, that is, the well-known 3%–3.5% of the required beam range. However, the error magnitude in the RSP conversion depends on the tissue type. Therefore the range margin for a specific beam should also depend on the types of tissues on the beam path and the path lengths through them. By investigating the range uncertainty issue specifically for each treatment site with its typical beam arrangement, we may be able to reduce the range margins with potential clinical benefits.

The motivation of this study is to develop a feasible method for conducting research on site-specific proton beam range uncertainty. The results of this study were clearly relevant only to the prostate treatments technique at MGH. However, we believe that the general approach demonstrated here could be beneficial to future studies on site-specific range uncertainty of other treatment sites. A limitation of the study arises from the clear differences between the selected animal tissues and human tissues in their radiological properties. The differences could be caused by tissue property difference and tissue excision. Given their small magnitudes (around 1%), the effect should be negligible on the main conclusions of the study.

In this study, small misalignments between the theoretically predicted and measured WEPL maps (figure 8) could happen because of phantom positioning errors when calculating the percentage WEPL differences (figures 9 and 10), although the virtual phantoms used by theoretical WEPL prediction methods (i.e. TOPAS and ray-tracing) were set up under the same three-dimensional coordinate system exactly as in the dose extinction

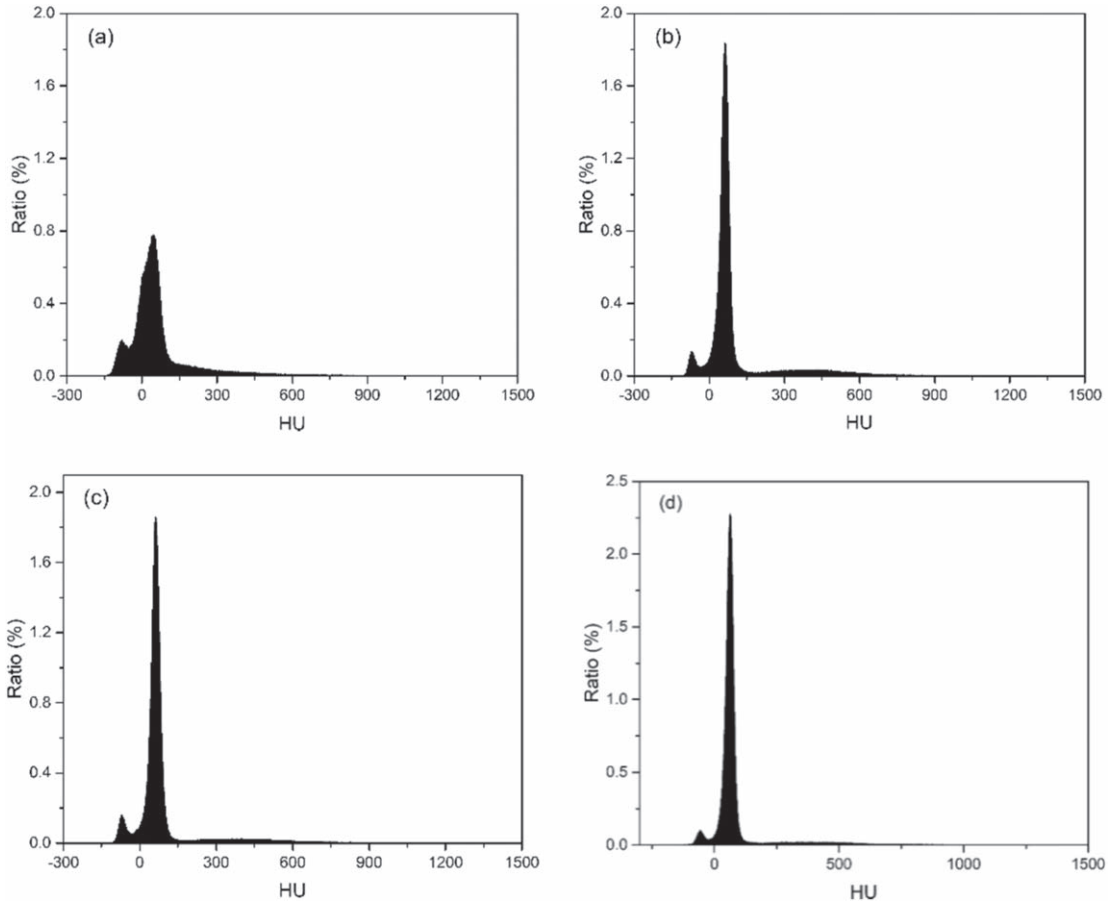

Figure 12. Histograms of CT HUs in percentage from the irradiated regions for (a) a real prostate patient, and (b), (c) for the three pelvic phantoms, respectively.

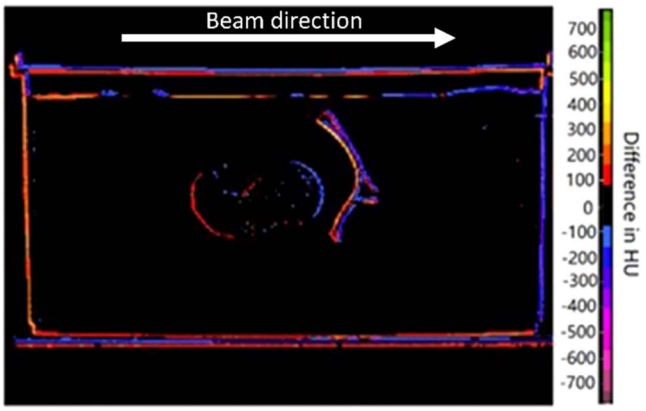

Figure 13. CT HU difference between the pre-experiment and post-experiment phantom 3.

experiment. The small misalignments from positioning errors were unavoidable in proton therapy for prostate cancer and mainly resulted in the large percentage WEPL difference between theoretical prediction and measurement around the sharp bone edge because of the large WEPL gradient (Farace *et al* 2016). The proton beam range uncertainties of this study included the effects of CT HU to RSP conversion uncertainty and misalignments from positioning errors. Thus, the results of this study could reveal the real proton range uncertainty in clinical proton therapy as much as possible. At present, the 3.5% range uncertainty from CT HU to RSP conversion and dose calculation uncertainty is applied in the clinic. However, the results of this study showed that proton beam range uncertainty was less than 2.5% even when CT HU to RSP conversion uncertainty,dose calculation uncertainty and misalignments from positioning errors coexisted. In the future,

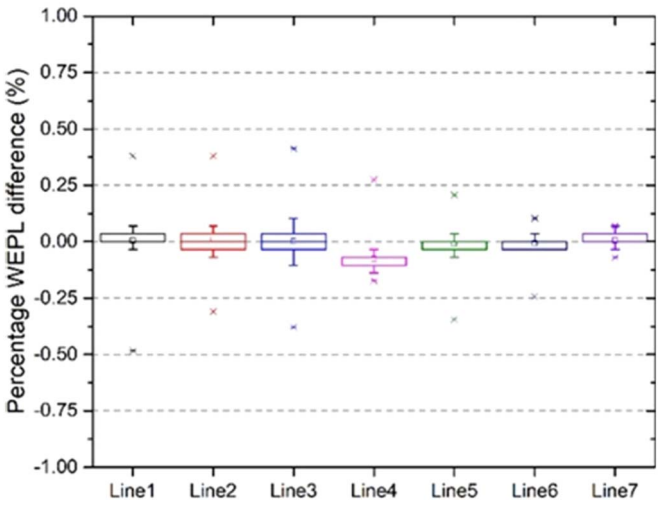

Figure 14. Box plots for the percentage WEPL difference between the ray-tracing-predicted WEPLs of the pre-experiment phantom and post-experiment phantom.

advanced image alignment procedures are recommended to be investigated and applied to reduce the range uncertainty around sharp bone edges as much as possible.

For furtherly verifying the phantom stability during the dose extinction experiments, ray-tracing WEPL calculation was also performed on the post-experimental CT scan of phantom 3 using the same method. Then the differences between the calculated WEPLs from both the pre- and post-experimental CT scans were obtained and shown in figure 14. As shown in figure 14, the maximal percentage WEPL difference was less than 0.5%, and the mean percentage WEPL difference was less than 0.25%. This suggests that the phantoms were reasonably stable during the experimental setup and dose extinction experiments. To keep the animal tissues within the biological phantom stable during the experiments, the animal tissues could be frozen or immersed in salt water with 0.9% salt concentration (Zhang *et al* 2017, Xie *et al* 2018). Freezing the animal tissues should be applied when the experiment did not cost much time to be accomplished. In this study, the dose extinction experiment for each phantom took more than 30 min. A lot of water drips could appear on phantom surfaces if the phantom was frozen. This occurrence could make the measured WEPLs unreliable. Thus, the animal tissues in the pelvic-like phantom were immersed in salt water with 0.9% salt concentration without being frozen to make the phantom as stable as possible during the dose extinction experiment.

The proton beams used in prostate treatments pass through sharp bone edges before reaching the prostate target volume. The results of this study shows that TOPAS MC is more accurate in predicting proton ranges than ray-tracing when sharp bone edges are involved. Moreover, the maximal WEPL discrepancy with measured WEPL for TOPAS MC was smaller than that for ray-tracing by at least 0.8%. Thus TOPAS MC has the potential to help proton TPS reduce the range margin accounting for proton range uncertainty. To achieve this, the WEPL through a prostate patient should be computed by TOPAS MC simulation, according to the virtual dose extinction experiment process proposed by this study. Thereafter, the region-dependent range margin from TOPAS MC needs to be applied instead of uniform 3.5% range margin during treatment planning. The range margin verification of this kind by TOPAS MC could reduce the dose to surrounding tissues in prostate treatments.

5. Conclusions

To date, a uniform range uncertainty of 3.5% + 1–3 mm is applied in clinical practice in proton therapy. We propose site-specific characterization of range uncertainties and performed a study for typical prostate treatment by lateral beams. We used pelvic-like biological phantoms and found that the difference between measured and theoretically predicted WEPLs is less than 2.5% depending on the tissue types through which proton beams pass. This suggests that the current 3.5% range uncertainty has the potential to be reduced by 1% even for single-energy CT and ray-tracing dose calculations in prostate treatments.

Acknowledgments

We would like to thank Douglas Trenholm and Caitlin Finley for the technical assistance during the dose extinction experiments. The authors do not have any conflicts of interests to disclose.

ORCID iDs

Wencheng Shao https://orcid.org/0000-0002-9109-5361
Jianan Wu https://orcid.org/0000-0003-3207-965X
Schuemann Jan https://orcid.org/0000-0002-7554-8818

References

Ainsley C G and Yeager C M 2014 Practical considerations in the calibration of CT scanners for proton therapy *J. Appl. Clin. Med. Phys.* **15** 202–20
Al-Abdin O Z and Al-Beeshi I Z 2018 Prostate cancer in the Arab population *Saudi Med. J.* **39** 453–8
Betefour H, Tang S, Cascio E W, Testa M, Samuel D, Prieels D, Gottsschalk B and Lu H M 2015 Validation of an *in vivo* proton beam range check method in an anthropomorphic pelvic phantom using dose measurements *Med. Phys.* **42** 1936–47
Brousmiche S, Souris K, de Xivry J O, Lee J A, Macq B and Seco J 2017 Combined influence of CT random noise and HU-RSP calibration curve nonlinearities on proton range systematic errors *Phys. Med. Biol.* **62** 8226–45
De Marzi L, Lesven C, Ferrand R, Sage J, Boulé T and Mazal A 2013 Calibration of CT Hounsfield units for proton therapy treatment planning: use of kilovoltage and megavoltage images and comparison of parameterized methods *Phys. Med. Biol.* **58** 4255–76
Doolan P J, Testa M, Sharp G, Bentefour E H, Royle G and Lu H M 2015 Patient-specific stopping power calibration for proton therapy planning based on single-detector proton radiography *Phys. Med. Biol.* **60** 1901–17
Farace P, Righetto R, Deffet S, Meijers A and Vander Stappen F 2016 A direct ray-tracing method to compute integral depth dose in pencil beam proton radiography with a multilayer ionization chamber *Med. Phys.* **43** 6405–12
Góes J A P *et al* 2018 Trend and spatial analysis of prostate cancer mortality in the state of Sergipe, Brazil *Geospat. Health* **13** 353–8
Guan F *et al* 2015 Analysis of the track- and dose-averaged LET and LET spectra in proton therapy using the geant4 Monte Carlo code *Med. Phys.* **42** 6234–47
Jiang H, Seco J and Paganetti H 2007 Effects of Hounsfield number conversion on CT based proton Monte Carlo dose calculations *Med. Phys.* **34** 1439–49
Joachim C *et al* 2018 Pattern of care of prostate cancer patients across the Martinique: results of a population-based study in the Caribbean *BMC Cancer* **18** 1130
Liebl J, Paganetti H, Zhu M and Winey B A 2014 The influence of patient positioning uncertainties in proton radiotherapy on proton range and dose distributions *Med. Phys.* **41** 091711
Mendenhall N P *et al* 2012 Early outcomes from three prospective trials of image-guided proton therapy for prostate cancer *Int. J. Radiat. Oncol. Biol. Phys.* **82** 213–21
Paganetti H 2012 Range uncertainties in proton therapy and the role of Monte Carlo simulations *Phys. Med. Biol.* **57** R99–117
Paganetti H and Kooy H 2014 Proton radiation in the management of localized cancer *Expert Rev. Med. Devices* **7** 275–85
Schneider W, Bortfeld T and Schlegel W 2000 Correlation between CT numbers and tissue parameters needed for Monte Carlo simulations of clinical dose distributions *Phys. Med. Biol.* **45** 459–78
Schuemann J, Dowdell S, Grassberger C, Min C H and Paganetti H 2014 Site-specific range uncertainties caused by dose calculation algorithms for proton therapy *Phys. Med. Biol.* **59** 4007–31
Shao W, Tang X, Bai Y, Geng C, Shu D, Gong C and Chen D 2017 Modulation of lateral positions of Bragg peaks via magnetic fields inside cancer patients: toward magnetic field modulated proton therapy *Med. Phys.* **44** 5325–38
Tryggestad E J, Liu W, Pepin M D, Hallemeier C L and Sio T T 2020 Managing treatment-related uncertainties in proton beam radiotherapy for gastrointestinal cancers *J. Gastrointest Oncol.* **11** 212–24
Testa M., Schümann J., Lu H.-M., Shin J., Faddegon B., Perl J. and Paganetti H. 2013 Experimental validation of the TOPAS Monte Carlo system for passive scattering proton therapy *Medical Physics* **40** 121719
Wang H, Wu J, Zhang R, Baer E, Geng C, Jee K, Sharp G, Paganetti H, Tang J and Lu H M 2017 Validation of Monte-Carlo proton dose calculation for real tissue samples: SU-I-GPD-T-119. AAPM 2017 Annual Meeting, Denver, CO, 7/30-8/4/2017 *Med. Phys.* **44** 2853
Xie Y *et al* 2018 *Ex vivo* validation of a stoichiometric dual energy CT proton stopping power ratio calibration *Phys. Med. Biol.* **63** 055016
Yang M, Zhu X R, Park P C, Titt U, Mohan R, Virshup G, Clayton J E and Dong L 2012 Comprehensive analysis of proton range uncertainties related to patient stopping-power-ratio estimation using the stoichiometric calibration *Phys. Med. Biol.* **57** 4095–115
Zhang R, Baer E, Jee K, Sharp G C, Flanz J and Lu H M 2017 Investigation of real tissue water equivalent path lengths using an efficient dose extinction method *Phys. Med. Biol.* **62** 5640–51
Zheng Y, Kang Y, Zeidan O and Schreuder N 2016 An end-to-end assessment of range uncertainty in proton therapy using animal tissues *Phys. Med. Biol.* **61** 8010–24